Flow through Channels with Deformable Obstructions

John Samuelsson, Mentors: Prof. Beverley McKeon and Dr. Mitul Luhar

***Abstract*—In this project, the static and dynamic deformation of deformable obstructions in confined flows was investigated via laboratory experiments. Flexible polyethylene walls of varying thickness were placed normal to the water flow in the Cann Water Tunnel, with flow speed estimated using Digital Particle Image Velocimetry, DPIV. The deformation was then captured using digital videography across a range of flow speeds.**

Unlike flexible bodies in unconfined flows, the Cauchy number, Ca, was not able to predict posture in steady state wall deformation. However, a modified Cauchy number taking the increase in velocity due to flow confinement into account, Ca^*, was sufficient for predicting posture for all wall lengths not exceeding the channel width. For walls of length longer than the channel width, self-similarity was broken and the deflected height of the flap converged to a constant value. That value was also predictable by Ca^*.

Experiments indicated that dynamic deformation occurs when Ca^* is typically larger than 3000 and the Reynolds number, Re, typically larger than 10000. The dynamic deformation was in the form of monofrequent oscillations with clear harmonic tendencies. The oscillations were vortex-induced with a Strouhal number, St, of 0.12.

I. Introduction

Many internal flows of biological and engineering interests are characterized by the presence of deformable obstructions, see Figure 1 [Vogel, 1996]. In such cases, interaction between the fluid flow and the flexible obstruction can produce a rich range of static and dynamic behavior.

Recent analytical and experimental studies have considered the static reconfiguration of flexible structures in unconfined flows [Alben et al., 2002; Gosselin et al., 2010; Luhar and Nepf, 2011]. In these studies, the behavior of flexible bodies has been shown to depend on a dimensionless parameter known as the Cauchy number, Ca, which is defined as the ratio of the aerodynamic or hydrodynamic force on the flexible structure and the restoring force due to structure stiffness [Luhar and Nepf, 2011].

However, the primary goal of these studies has been to characterize the reduction in aerodynamic or hydrodynamic drag that results from the reconfiguration of flexible structures [Alben et al., 2002]. The effects of placing such flexible walls in confined channels, such that the structures obstruct the flow, have not been considered. To address this gap, the flow and deformation of a flexible body confining the flow were examined via laboratory experiments.

Our hypothesis was that in confined flows, where we expect a greater interaction between the body confining the flow and the fluid, the Cauchy number is not enough to predict behavior, but one also needs the confinement ratio,

$$Q = \frac{h}{w}, \tag{1}$$

where h is the deflected height of the body and w is the channel width. Other parameters that might have an influence in their own right include rigidity, R [Nm^2], and flow velocity along the tunnel, u [$\frac{m}{s}$], of the fluid. Throughout this paper, the coordinate system found in Figure 3 will be used. That is, $\boldsymbol{x}$ points along the length of the tunnel, $\boldsymbol{y}$ points in the direction perpendicular to the sidewall over the width of the channel, and $\boldsymbol{z}$ points from the bottom upwards. The (x, y, z) components of the velocity field of the fluid is defined as $\boldsymbol{u} = (u, v, w)$.

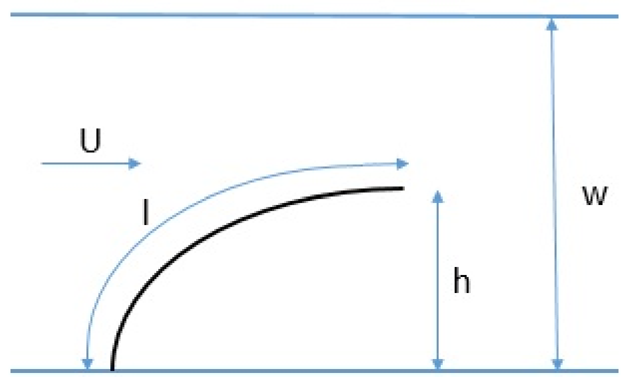

Figure 1. Model over investigated configuration. w represents channel width, h deflected height, l flap length and U the free stream velocity. The black line represents the flexible body bending by drag force, the initial state of the flap is vertical.

Background Theory

This section provides a brief review of the model developed by Luhar and Nepf (2011) describing the steady state posture of a flexible flap in an unconfined flow. This model is used to generate posture predictions in the following sections. The flap is modeled as a blade pin jointed at the bed with a free tip, see Figure 2. We use the curvilinear coordinate system shown in the same figure, in which s is the coordinate going along the flap from the base, so that $s = 0$ represents the bed and $s = l$ the tip. $\theta(s)$ represents the angle with the vertical plane and U the free stream velocity. Observing force balance for the part of the blade from s^* to the tip, where s^* is any value of

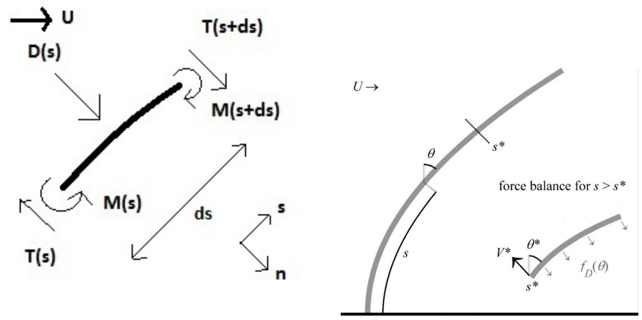

Figure 2. Model over flap in bent state. Picture to the left shows forces and torque acting on a small part ds of the flap. Picture to the right shows a schematic over the curvilinear system and inset used to derive mathematical model [Luhar and Nepf, 2011].

s from 0 to l, we have two forces at work: the restoring force due structure stiffness, $V^*(s^*)$, and drag $f_D(\theta)$, see Figure 2. Observing a part of the flap ds (see Figure 2), the torque balance equation gives,

$$\frac{1}{2}ds(T(s)+T(s+ds)) - M(s) + M(s+ds) = 0$$

$$\Rightarrow T(s) \cong -\frac{dM(s)}{ds}$$

$$M(s) = EI\frac{d\theta}{ds} \Rightarrow T(s) = -EI\frac{d^2\theta}{ds^2},$$

where E is the elastic modulus of the flap, I the second moment of inertia with respect to the bending axis assuming plain bending, T the shear force and M the internal torque [Ludh, 2000]. In the inset in Figure 2, V^* is the shear force at $s = s^*$ so

$$V^* = T(s^*) = -EI\frac{d^2\theta}{ds^2}|_{s=s^*}.$$

The form drag exerted by the fluid on the body is represented by

$$f_D = \frac{1}{2}C_D\rho AU^2,$$

where ρ is the density of the fluid and A the area normal to the water flow [Blevins, 1984]. Assuming skin friction to be negligible in relation to form drag, we neglect the velocity component tangential to the flap and only include the velocity component normal to the flap. The drag for a part ds of the flap is then

$$f_D = \frac{1}{2}C_D\rho b ds U^2\cos^2(\theta),$$

where b is the depth of the flap and C_D the drag coefficient. The steady state force balance equation for the vector component normal to the wall for the inset is then,

$$\boldsymbol{n}: \; V^* + f_D = 0$$

$$-EI\frac{d^2\theta}{ds^2}|_{s=s^*} + \int_{s^*}^{l}\frac{1}{2}C_D\rho bU^2\cos^2(\theta)\cos(\theta-\theta^*)\,ds = 0$$

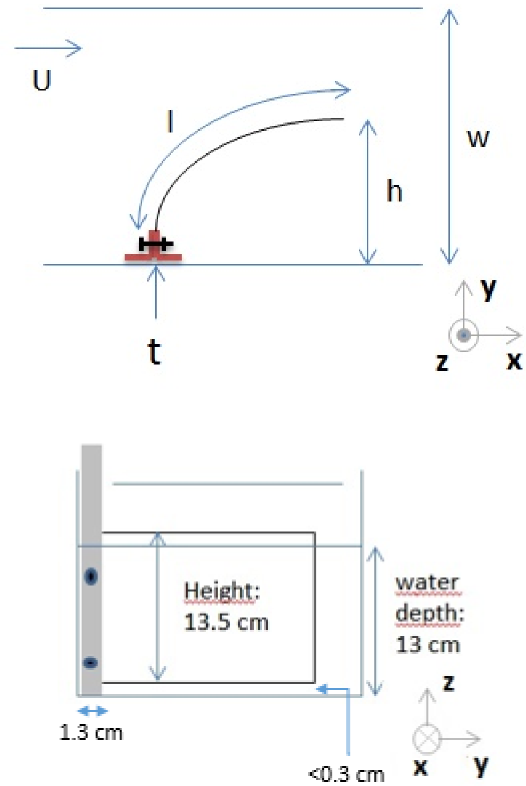

Figure 3. Experimental setup. The flap is being held in place by two angle bars, one at each side, pierced by two screws. Schematic not to scale.

Normalizing the s-coordinate via $\hat{s} = \frac{s}{l}$, so that $\hat{s} = 0$ represents the base and $\hat{s} = 1$ the tip of the flape, we have

$$-\frac{EI}{l^2}\frac{d^2\theta}{d\hat{s}^2}|_{\hat{s}=\hat{s}^*} + \int_{\hat{s}^*}^{1}\frac{1}{2}lC_D\rho bU^2\cos^2(\theta)\cos(\theta-\theta^*)\,d\hat{s} = 0.$$

$$-\frac{d^2\theta}{d\hat{s}^2}|_{\hat{s}=\hat{s}^*} + \frac{l^3C_D\rho bU^2}{2EI}\int_{\hat{s}^*}^{1}\cos^2(\theta)\cos(\theta-\theta^*)\,d\hat{s} = 0.$$

By letting the Cauchy number, Ca, be represented by

$$Ca = \frac{l^3C_D\rho bU^2}{2EI} \tag{2}$$

we get the final expression of the force balance equation,

$$-\frac{d^2\theta}{d\hat{s}^2}|_{\hat{s}=\hat{s}^*} + Ca\int_{\hat{s}^*}^{1}\cos^2(\theta)\cos(\theta-\theta^*)\,d\hat{s} = 0.$$

For a wall of rectangular cross section, $I = \frac{1}{12}bt^3$ and our Cauchy number becomes $Ca = \frac{6l^3\rho bC_D}{Et^3}$ [Sundström et al., 1998]. This equation can be solved numerically using an iterative shooting method with the boundary conditions $\theta(0) = 0$ and $\frac{d\theta}{d\hat{s}}|_{\hat{s}=1} = 0$. Doing so yields the angle θ at all positions along the blade and by that the posture is determined. Since Ca is the only parameter needed to solve

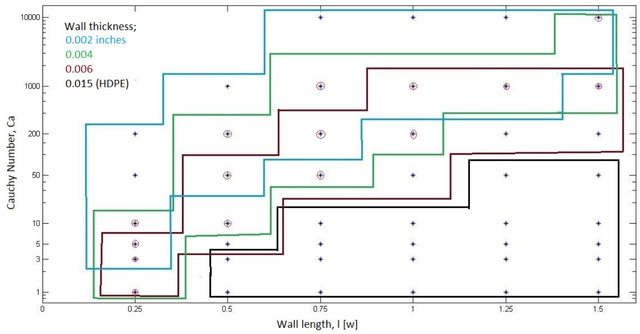

$\frac{l}{w}$	Flow velocities, u [$\frac{cm}{s}$]				
1/4	21.1*	10.5*	4.7*	13.3**	9.4**
	7.3**	4.2**	17.3***	13.4***	7.7***
2/4	11.9*	5.3*	15.1**	7.6**	3.4**
	13.9***	6.2***	4.4***	11.6****	26.5****
3/4	18.7*	5.9*	16.7**	7.4**	3.7**
	13.7***	6.8***	23.9****	6.3****	14.2****
	20****				
1	11.6*	3.7*	10.4**	4.6**	8.5***
	4.3***	4.1****	7.5****	20.6****	
5/4	8.0*	7.2**	13.3***	5.9***	23.1****
	10.4****	7.3****	5.6****	3.3****	
6/4	6.0*	17.0**	5.4**	9.9***	4.4***
	17.3****	7.7****	5.5****	4.3****	2.5****

Figure 4. Obtainable measuring points in $(Ca, \frac{l}{w})$-space for different walls. Walls of thickness 0.002, 0.004, 0.006 inches are all of LDPE, the 0.015 ich wall is of HDPE. Conducted measurments are marked as stars in the plot, stars with circles around them were made twice for different values of rigidity (i.e. different walls) and flow velocities. * = wall thickness 0.002", ** = wall thickness 0.004", *** = wall thickness 0.006", **** = wall thickness 0.015".

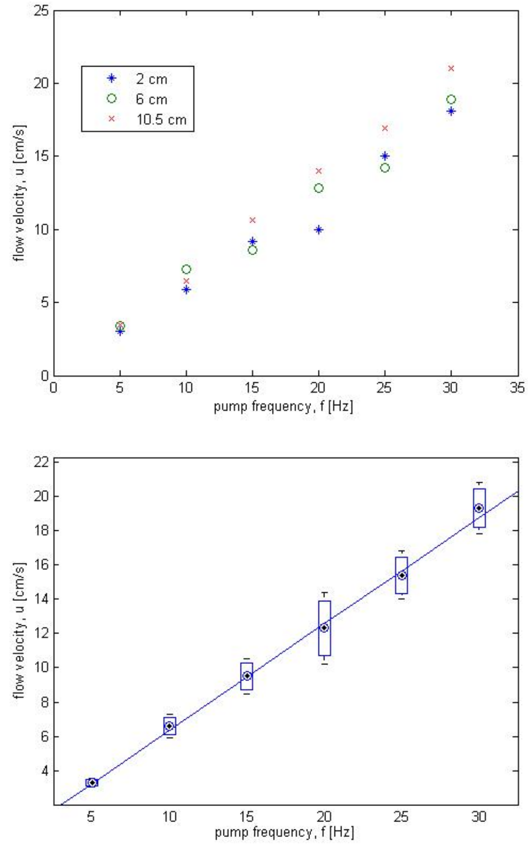

Figure 5. Flow velocity vs pump frequency for different heights (to the left) and the average flow velocity for given pump frequencies (to the right) along with a linear least square fit. The points represents the average and the boxes the standard deviation.

the equation, and thus finding the posture, Ca is the sole parameter governing posture. Another important observation is that the length of the flap only goes into the equation via the Cauchy number. Thus, if two flaps of different lengths have the same Cauchy number, the deformation will be identical up to a matter of scaling. In other words, the normalized height of the flaps, $\frac{h}{l}$, will be identical for the same Cauchy number. Therefore we say that the bending is self-similar.

When the Cauchy number is larger than 1, the drag is stronger in relation to structure stiffness and the flap bends over more. As the flap becomes increasingly bent, the deflected height h becomes smaller. Given that the bending is self-similar, there is a one-to-one relationship between Ca, the flap posture, and the scaled deflected height, $\frac{h}{l}$. Therefore, $\frac{h}{l}$ is a good metric for comparing deformation across all cases, where a larger deformation means a smaller value of $\frac{h}{l}$.

II. Methodology

Experiments were conducted in the Graduate Aerospace Laboratories of the California Institute of Technology, in the CANN water tunnel. The water tunnel has a 15.7×14.5 cm cross section, a 79 cm long test section and is fitted with a variable speed pump. Throughout this study, a water level of 13.0 cm was used. Prior to performing the deformable wall experiments, a velocity calibration of the GALCIT water tunnel was made. The study used DPIV technique to find the velocity field of the fluid. A 1 W continuous laser was used for illumination and a 1280×1024 pixel CCD camera was used to record images at $60-100$ frames/second (fps). The camera was placed around 45 cm down the length of the test section. The water was seeded with particles of density 1.1 $\frac{g}{cm^3}$ (type AgSL150-30-TRD, by Potters Industries). The images were analysed and the velocity field of the fluid found by using PIVlab software package [http://pivlab.blogspot.com].

Water Tunnel Calibration

PIV measurements were made at three different heights above the bottom of the channel: $z = 2$, 6 and 10.5 cm and at pump frequencies of 5–30 Hz with a linear unit step of 5 Hz, making a total of 18 measurements. The PIV algorithm used Direct Cross Correlation (DCC) with a highpass filter of size 15 pixels, and an interrogation area of 90 pixels. While post processing the data, extremely deviating velocity vectors, defined as those deviating more than 7 standard deviations relative to the surrounding vectors, were discarded and replaced with vectors found from interpolation. A calibration image of an object (a ruler) of known size was taken and uploaded at each height to give physical dimensions to the flow. Mean flow

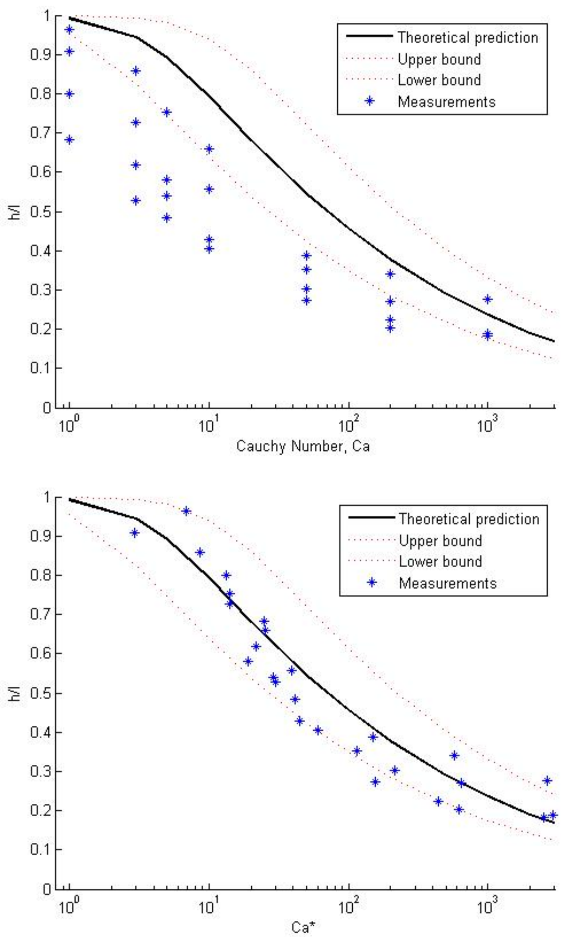

Figure 6. Measurements and theoretical prediction with error bars of $\frac{h}{l}$ plotted to Cauchy number. In the picture below, the Cauchy number of the measurements have been replaced with Ca^* based on measured deflected height h.

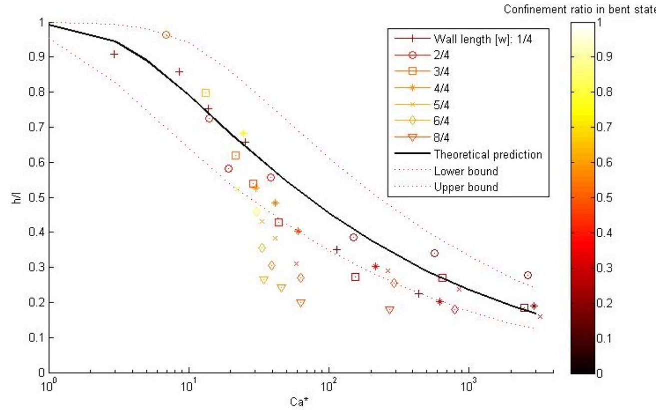

Figure 7. $\frac{h}{l}$ plotted to Ca^* for all performed experiments, each point represents one experiment. The marker represents wall length and the color of the marker represents confinement raito.

vectors were calculated over all the frames, and the average flow velocity of all the cubes in the mean frame was taken as the flow velocity u.

Static Deformation

The aim of the experiment was to investigate wall deformation when the wall is flexible and confining the flow, as well as the transition from the unconfined to confined case. For simplicity we wanted to make the experiment two dimensional ($2d - 2c$), i.e. having no z-dependency in the flow and wall deformation as well as keeping w at zero. This was achieved by having the flexible wall ending just above the water surface. To ensure that the water was not going over the wall and thus leading to a non-zero w velocity, the wall extended 5 mm above the water surface, see Figure 3. The change in flow velocity u and confinement ratio q under the course of the experiment led to small variations in water depth. However, the maximum difference for relevent flow rates was around 2 mm, so having a 5 mm margin ensured water not flowing over the wall. We assume that the z-dependency in the wall deformation induced by having water pressure in the wetted portion and no pressure in the part above the water surface is negligible, since the wall was 135 mm of height, of which only 5 mm (3.7 %) was above the water surface. The wall ended $2 - 3$ mm over the bottom of the channel in order to make sure that no part of the wall was dragging the bottom, generating unwanted friction on the wall and thus disturbing the experiment.

Two angle bars held together by a screw and clamps were used to keep the wall in place. For the thinner walls, two screws had to be used in order for the flexible wall not to slip, in this case no clamps were needed. The friction between the bottom and the angle bars proved sufficient in keeping the construction in place, not sliding along the length of the water tunnel. When applying high flow velocities to the more rigid HDPE material, a greater drag was generated by the wall. For such cases, the construction was held in place using extra weights. The angle bars were of type Low-Carbon Steel 90 Degree Angle 1/2" X 1/2" Legs, 1/8" Wall Thickness, 1' Length. In order to determine whether the angle bars would remain rigid under the course of the experiment, its Cauchy number, $Ca = \frac{6\rho U^2 C_D l^3}{Eb^3}$, was calculated. Typically, a Cauchy number larger than 1 means it will bend over, while a Cauchy number smaller than 1 means it will stay firmly rigid. The angle bars have a Cauchy number in the order of 10^{-4}, ensuring their being rigid in the flow.

The investigated flexible walls were made of High Density Polyethylene, HDPE, and Low Density Polyethylene, LDPE. HDPE has a density of $\rho = 0.95 \ \frac{g}{cm^3}$, while LDPE has a density of $\rho = 0.92 \ \frac{g}{cm^3}$ so $\Delta\rho_{HDPE} = 0.05 \ \frac{g}{cm^3}$ and $\Delta\rho_{LDPE} = 0.08 \ \frac{g}{cm^3}$ in water. Thus the bouyancy of HDPE is much less than that of LDPE. However, because of its relatively high elastic modulus, $E_{HDPE} = 0.93$ GPa, the wall need to be very thin in order to get high Cauchy numbers for a given length. LDPE has an elastic modulus of $E_{LDPE} = 0.235$ GPa and homogenous, pure LDPE sheets are available in thickness starting at 0.002 inches, which allows larger Cauchy numbers.

In order to get the buoyancy negligible for the LDPE material, which has a relatively large density difference to that

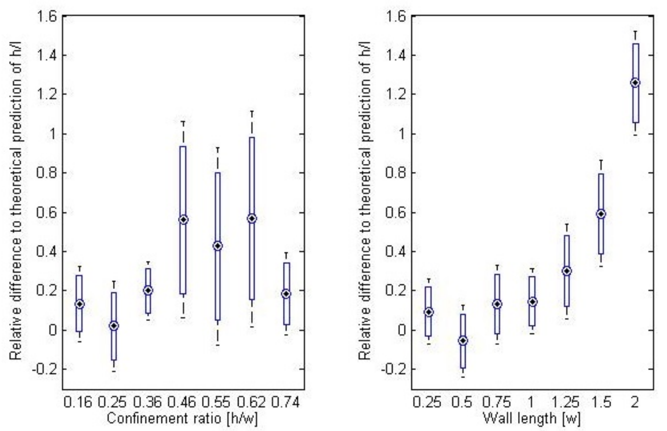

Figure 8. Relative difference of experimental value of $\frac{h}{l}$ to theoretical prediction, plotted versus confinement ratio and wall length. Measurements have been grouped together in intervals of 0.1, from $(0.1, 0.2)$ to $(0.6, 0.7)$ in the case of confinement ratio (left plot). The circles represent the average value and the flyers plus/minus one standard deviation in the relevant interval. The average value of the confinement ratio in the interval has been written out on the x-axis.

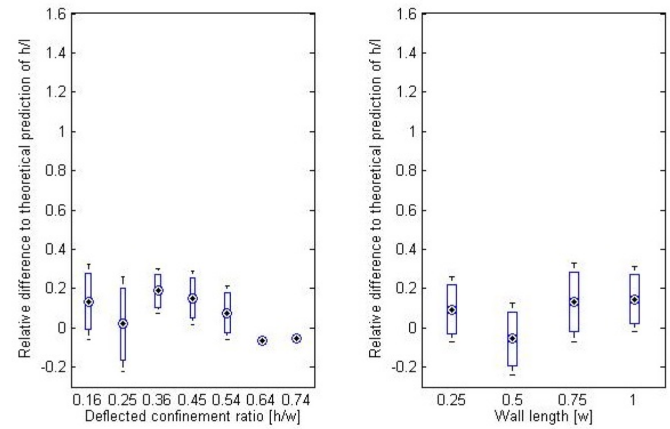

Figure 9. Same plot as Figure 8, excluding walls longer than channel width.

of water, the ratio of the drag force to the restoring force due to buoyancy has to be big, so that the wall is pushed back into the non-buoyant deformation state by the drag force when it tries to bend itself upward due to buoyancy. Specifically, the ratio of drag force to buoyancy force is equal to the ratio of the Cauchy number to the buoyancy parameter, defined as

$$B = \frac{\Delta\rho g t l^3}{EI},$$

since $Ca = \frac{Drag\ force}{Stiffness\ force}$ and $B = \frac{Boyancy\ force}{Stiffness\ force}$, so $Ca \times B^{-1} = \frac{Drag\ force}{Stiffness\ force} \times \frac{Stiffness\ force}{Boyancy\ force} = \frac{Drag\ force}{Boyancy\ force}$. If $Ca \times B^{-1} \geq 10$, the buoyancy can be neglected with high precision [Luhar and Nepf, 2011]. Thus we had to make sure that

$$Ca \times B^{-1} = \frac{0.5\rho C_D U^2}{\Delta\rho g t} \geq 10 \Leftrightarrow U \geq \sqrt{\frac{20\Delta\rho g t}{\rho C_D}},$$

where $g = 9.8\ \frac{m}{s^2}$ is the gravity constant and $\rho = 1.0\ \frac{g}{cm^3}$ the density of water for each tested wall.

The range of flow velocity in the water tunnel was $u \in (2.5, 25)\ \frac{cm}{s}$. One HDPE wall of thickness 0.015 inches and three LDPE walls of thickness 0.002, 0.004, 0.006 inches were used. Taking all these limitations into account, the obtainable measurement points in $(Ca, \frac{l}{w})$ − space are as shown in Figure 4. Since our hypothesis is that the confinement ratio and the Cauchy number are the two parameters that dictate posture, we want to investigate the dependency of these in the deformation. Therefore the measurement points represent isolines for Ca and $\frac{l}{w}$. Further, in order to see whether Ca and $\frac{l}{w}$ are sufficient in predicting posture, we kept Ca and $\frac{l}{w}$ constant while varying rigidity and flow velocity for different points in $(Ca, \frac{l}{w})$-space. All measurements are found in the tables in Figure 4, which shows that the wall length varies between a quarter of the channel width, 0.25 w, to 1.5 w. For given wall lengths we are able to vary flow speed and through that vary Ca. For current constraints the range of Ca goes form $1 - 200$ to $1 - 10000$. Secondary measurements were made of wall length $2\ w$ for Cauchy Numbers $Ca = 3, 5, 10, 50, 200, 1000, 10000$.

The deformation of the wall was found using a grid at the bottom of the water tunnel. In the cases of longer walls, the camera had to be moved along the length of the water tunnel to capture the whole deformation. Because of the limited bandwidth of the camera, a high frame rate and a full 1280×1024 resolution was not obtainable. Because of this, at high flow velocities where the PIV analysis requires a high frame rate, the image was split in smaller sections during the recording and then later merged together to get the full picture.

Dynamic Deformation

To investigate what parameters dictating the transition into oscillatory state, LDPE-flaps of thickness 0.002 and 0.004 inches and lengths varying from $\frac{2}{4}$ to $\frac{6}{4}$ w with an interval of $\frac{1}{4}w$ were used. The flaps were immersed into still water, one at a time, after which the flow velocity was slowly increased until the flap started oscillating. The flow velocity was then decreased until the flap went back into steady state. Both of these transition speeds were noted. Two different definitions of oscillations were used: absolute and relative oscillations. In the case of absolute oscillations, the oscillation of the tip of the flap had to be of at least 1 cm amplitude. In the relative case, the amplitude of the tip had to be $\frac{l}{w}$ cm. Experiments showed, however, that the relative and absolute case led to similar results for the transition speed.

Once the flap had reached oscillatory state, the deformation was recorded. The video was then converted into an image sequence using Image-J software package. A point of the flap defined as the point closest to the tip where the angle θ never went above 90^0 (i.e., never pointed towards the wall to which the flap was attached) was being tracked by cutting the images, making them vertical, at this point. The images were then loaded into Matlab and converted into grayscale, so that each pixel had a numerical value of $0 - 1$ where 1 represented a completely white and 0 a completely black pixel. In order to find the flexible wall, which was lit up white by laser

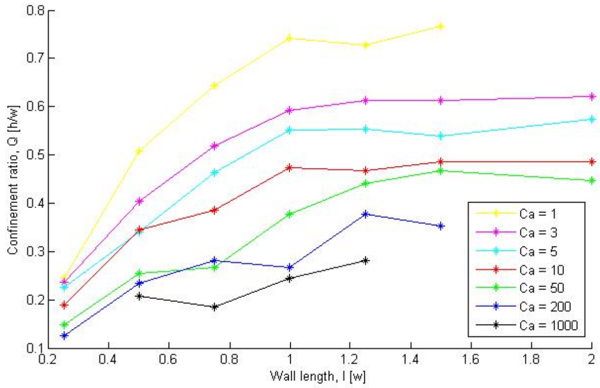

Figure 10. Confinement ratio plotted to wall length, measurements of the same Cauchy number have been given the same color.

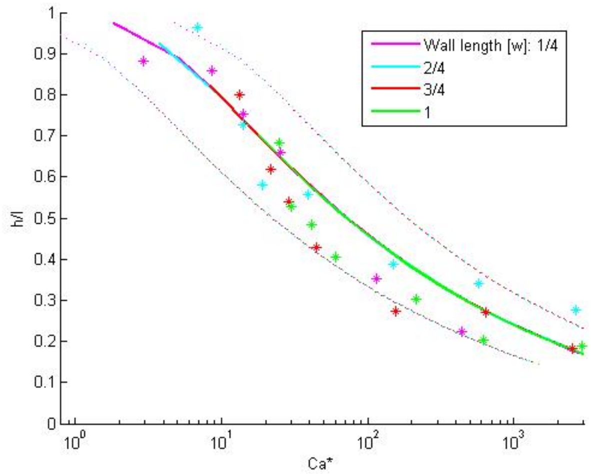

Figure 11. Measurements and *purely* theoretical prediction in $(\frac{h}{l}, Ca^*)$-space, error bars included as dashed lines. The theoretical predictions converge, as expected, for walls of varying lengths.

illumination, a pixel was defined as white if its grayscale value was at least 95% of the maximum value in the current picture. Since the water was seeded by illuminated, white particles, it was not trivial finding the flap. To overcome this, the vertical coordinate (the y-coordinate) of all the "white" pixels (i.e., both the particles and the flap) were saved into a vector and the flap was found by taking the median value of this sorted vector. The median value was then saved as the y-coordinate of the flap. This process was repeated for all the pictures, saving the position of the flap at different times, after which plots over amplitude versus time were obtainable.

III. Results

Water Tunnel Calibration

The calibration results of the velocity calibration are shown in Figure 5. Observing the results, one sees that there does not seem to be any systematic difference in velocity at different depths, so variations are assumed to be random and velocity profile uniform within tested water depths. Therefore an average was taken of the all the measurements at each given frequency and a linear least square fit was applied to this data. The result was the linear equation $u = 0.62f + 0.15$, where u [$\frac{m}{s}$] is flow velocity and f [Hz] pump frequency, with an R2 –value of 0.9972. Figure 5 also shows the average values over depth at given frequencies along with a confidence interval taken as plus/minus one standard deviation of the data acquired at each frequency, as well as the result of the linear regression.

One might expect that the velocity profile of u would change over the tunnel width with no slip boundary conditions at the sidewalls. However an analysis shows that even though the velocity profile was not perfectly uniform across the width of the channel, there was no profile that repeated itself over different measurements, and so the non-uniformity in the profile is accredited to random error, which is reasonable considering the small difference to the mean velocity u of typically less than 5 %.

Static Deformation

As we originally anticipated, the Cauchy number is not sufficient for predicting posture for flexible bodies in confined flows, see Figure 6. As expected, the error grows with longer wall length. The best prediction is the one made for the shortest flap of length $l = \frac{1}{4}w$ where 5 out of 6 measurements are within the error bounds. The error bounds correspond to the uncertainty of the Cauchy number (e.g. due to material property and wall thickness variations). The largest source of error was the wall thickness and so the Cauchy number ranged from $0.32 - 2.6$ of the estimated value. These uncertainty estimates are quite conservative, the upper bound of all possible sources of error has been used. Thus it would be logical to let each measurement be represented by a horizontal box, stretching from the upper to the lower bound of Ca. In the interest of accessibility, however, we will reframe from doing so and instead set these bounds on the theoretical prediction.

In order to make a better prediction that is taking the confinement into account, we replace the free stream velocity U in the Cauchy number (2) for the velocity of the fluid as it passes the tip, u_2. Due to the incompressibility of water, the flow speed will increase so that $u_2 = \frac{U}{(1-Q)}$ where $Q = \frac{h}{w}$ is the confinement ratio and u_2 the flow speed at the tip of the flap. Thus, a modified Cauchy number can be defined as

$$Ca^* = \frac{l^3 C_D \rho b u_2^2}{2EI} = \frac{l^3 C_D \rho b U^2}{2EI} \frac{1}{(1-Q)^2} = \frac{Ca}{(1-Q)^2}. \tag{3}$$

Using this number, we get the results shown in the lower picture of Figure 6, which shows walls of lengths $l \leq w$, where all but two measurements fall within the error bars of the prediction.

In Figure 7 all the conducted measurements are found in one plot. There is a family of measurements lying considerably under the error bars of the theoretical predictions. All of those have one common factor - they are all walls of length longer than channel width, $l > w$. Another observation is that there is a rich range of marker colors lying within the error bars. Thus it seems as though Ca^* makes up for confinement ratio Q in an excellent manner, but fall short when the walls grow longer

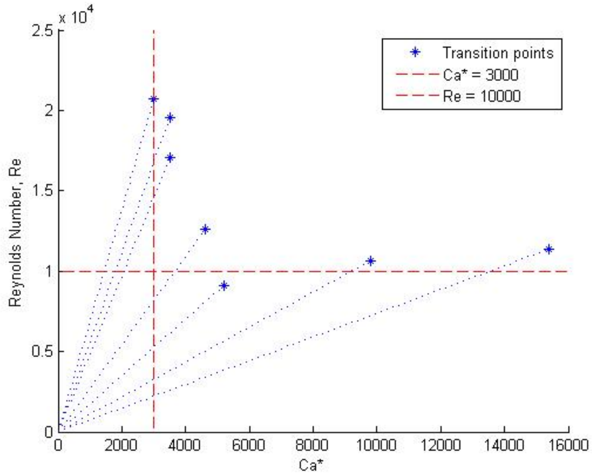

Figure 12. Dynamic measurements in (Re, Ca^*)-space. While performing experiments, we were walking along the dashed lines away from the origine until we reached oscillatory motion. The points at which the flap started oscillating are marked with blue stars.

than channel width. Both of these observations are confirmed in Figure 8. Here there is a clear break point between walls of length w and $\frac{5}{4}w$, when $l \leq w$ the relative error is quite constant, but starts increasing with l when $l > w$. Looking at the picture to the left in Figure 8, there does not seem to be any real trend line over varying confinement ratio, the high median values in the upper intermediate regions of $Q \in (0.4, 0.7)$ owe to the longer walls that happen to be overrepresented in this region. This conclusion is confirmed by Figure 9 where we have removed walls of length longer than channel width.

Thus far we have concluded that Ca^* is sufficient for predicting $\frac{h}{l}$, and by that also posture, for wall lengths $l \leq w$ and all confinement ratios Q. When the flap grows longer than channel width, the self-similarity across walls of varying lengths is broken, as is shown in Figure 10 where $\frac{h}{w}$ is plotted to wall length. Since w is constant, any change in the y-coordinate is accredited to a change in deflected height h. Easily observable, there is a clear transition between $l \leq w$ and $l > \frac{5}{4}w$ where the isolines for Ca goes from scaling roughly linearly with wall length to becoming completely horizontal, converging to a constant value of h. Thus h scales with wall length, as it should for self-similar bending, before the transition point. After, however, h is constant as wall length increases for a constant Ca or Ca^*, meaning that the self-similarity is broken. However, the value of convergence is nothing but the value of h for wall length $l = w$, which is predictable using Ca^*. Thus h can be predicted by Ca^* for longer walls as well, as long as we change the prediction accordingly, i.e. the deflected height for flaps with $l > w$ and a given Ca^* is the same as that for flaps with $l = w$ with the same Ca^*. However, since the self-similarity does not hold for walls where $l > w$, posture is no longer uniquely defined by $\frac{h}{l}$ and so we cannot predict posture as we can when $l \leq w$. We can only predict deflected height h and through that obstruction ratio Q.

So far the experimental value of deflected height h has

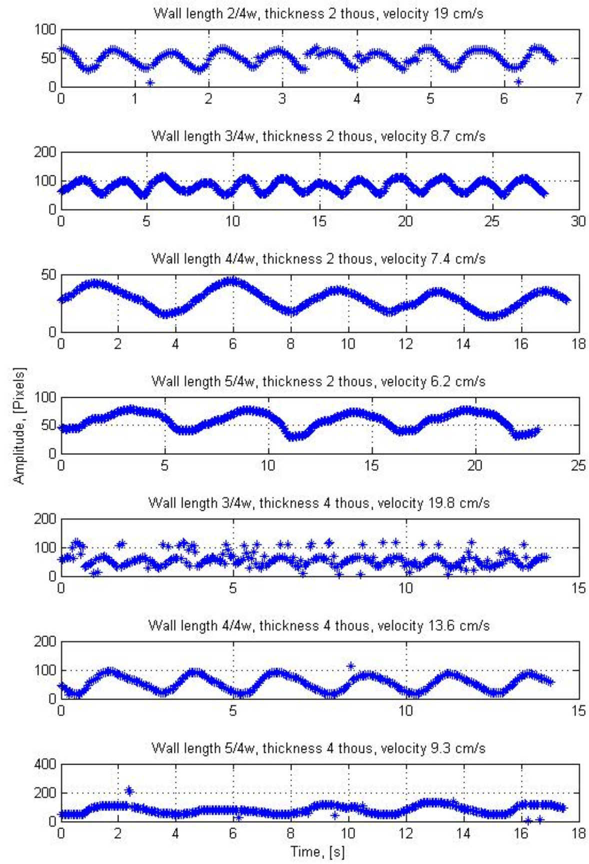

Figure 13. y-position of the tracked point versus time for oscillating flaps.

been used in order to find Ca^* for the flaps. Of course, the value of h is not known a priori. In order to make a purely theoretical prediction of the deflected height h, two parameters are needed; Ca, which is estimated based on known material and geometric properties of flap, and the confinement ratio in unbent state, i.e. wall length over channel width. To do this, an iterative algorithm was used where h was firstly calculated based on Ca. This value of deflected height h was then used to find Ca^*. Recalculating h based on Ca^*, a new value of h was found, leading to a new value of Ca^*. This process repeated itself until h converged, i.e.

$$Ca \rightarrow h_0 \rightarrow Ca_1^* \rightarrow h_1 \rightarrow Ca_2^* \rightarrow h_2 ...$$

Convergence was considered to be found when h did not change more than 1 % between two cycles. Using this algorithm, convergence was found for all walls not exceeding channel width, see Figure 11. No convergence was found in the case of walls longer than channel width, in these cases h circulated between a very high value, typically over 90 %, and a very low value, around 10 %. This is beacause a high value of Ca^* leads to a small h, which in turn leads to a small value of Ca^*, leading to a large h, leading to a large Ca^*

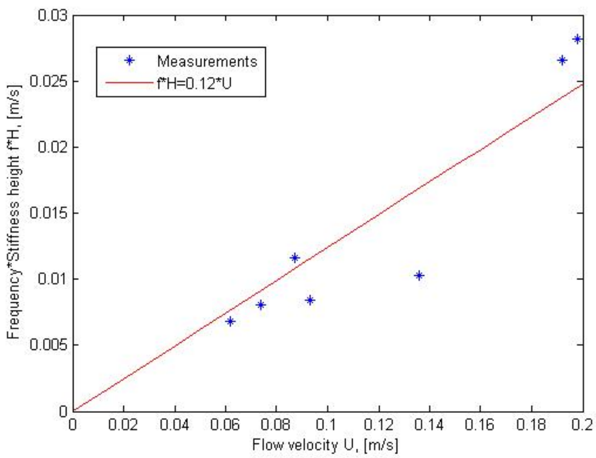

Figure 14. Frequency times stiffness height plotted to flow velocity with a linear least square fit. The slope of the fit is the Strouhal number, St.

and the loop starts over, i.e. h big $\rightarrow Ca^*$ big $\rightarrow h$ small $\rightarrow$ Ca^* small $\rightarrow h$ big....

Dynamic Deformation

Observing figure 12, there seem to be two dimensionless parameters determining the transition into oscillatory motion: Ca^* and Reynolds number, Re. $Re = \frac{UL}{\nu}$, where the characteristic length L is taken as the lengths of the flaps. Specifically, the requirements for dynamic deformation appear to be $Ca^* > 3000$ and $Re > 10000$, meaning the tranisition points should cluster up at the isolines $Re = 10000$ and $Ca^* = 3000$.

Observing the oscillations (see Figure 13), one clearly sees harmonic tendencies, but the oscillations do not seem to be purely sinusoidal, some of the oscillations look more like triangle waves. In some oscillations the upward motion takes more time than the downward motion, in other oscillations it is the other way around. The time interval between two neighboring peaks for each wall oscillation is nearly constant, thus the oscillations are near mono-frequent and this frequency is easily found by taking the inverse of the average time interval. Using this frequency, along with the stiffness height, defined as the average height over time of the tracked point of the flap over the wall, and the free stream velocity, we can find the Strouhal number, St. Plotting frequency times stiffness height versus flow velocity and applying a linear least square fit to the data on the form $y = ax$, we get an R^2-value of 0.85 and $a = 0.12$ (Figure 14). The a-parameter would be the Strouhal number, which we would expect to be somewhat under 0.2 if the oscillations are vortex-induced. The St value of 0.12 is thus indicative of a vortex-induced phenomenon and is roughly consistent with that expected for bluff bodies, $St < 0.2$.

The dependence on Ca^* has an intuitive physical interpretation - as the Ca^* parameter increases, the flap bends over more, increasing curvature near the base and decreasing curvature away from the bed, making the rest of the flap close to linear-shaped [Alben et al., 2002]. Since the restoring force due to structure stiffness is $F_{re} = -EI\frac{d^2\theta}{ds^2}$, the flap gets stiffer in the region closer to the bed and more flexible in the outer part as Ca^* increases until the shape resembles a rigid quarter of a cylinder with a straight, streamlined, flexible tail behind it. Once Ca^*has reached 3000, the flap will be sufficiently deformed so that the 'rigid' quarter cylinder near the base will vortex-shed downstream, the vorticity will induce a pressure difference to the surrounding fluid and push the 'flexible tail' from its streamlined position. This disturbance from the equilibrium position travels with the vorticity downstream, causing the flap to oscillate. The dependence on Re needs to be studied further.

IV. Conclusions and Future Work

In agreement with our hypothesis, the Cauchy number was not able to predict posture in steady state wall deformation. However, a modified Cauchy number taking the increase in velocity due to flow confinement into account, Ca^*, was sufficient for predicting posture for all wall lengths not exceeding the channel width. For walls of length longer than the channel width, self-similarity was broken and the deflected height of the flap converged to a constant value depending on the value of Ca^*. That value is also predictable by Ca^*, thus Ca^* is sufficient for predicting posture for wall lengths not exceeding channel width and obstruction ratio for all wall lengths.

Experiments indicated that dynamic deformation occurs when $Ca^*$is typically larger than 3000 and the Reynolds number, Re, typically larger than 10000. The dynamic deformation was in the form of monofrequent oscillations with clear harmonic tendencies. It appears that the oscillations are vortex-induced with a Strouhal number, St, of 0.12.

Future work on this area should include an analytical model for steady state wall deformation in confined flows explaining the importance of Ca^* and observed convergence in h. Further, since the primary interest of this topic is in internal biological flows and blood is a non-newtonian fluid, it would be interesting to investigate the case when the fluid is non-newtonian. For the same reason, in biological contexts one often see two flaps, one fastened at each wall, facing eachother over the channel (e.g. vocal cords and heart valves), therefore investigating the effect of such "double-flap" setup would be useful when trying to apply these results to real world problems.

V. References

- Alben, S., M. Shelley and J- Zhang (2002) Drag reduction through self-similar bending of a flexible body. Nature, 420: 479-481
- Blevins, R. D. (1984) Applied fluid dynamics handbook, Van Nostrand Reinhold
- Gosselin, F., E. de Langre, and B.A. Machado-Almeida (2010) Drag reduction of flexible plate by reconfiguration. Journal of Fluid Mechanics, 650: 319-341
- Luhar, M. and H. Nepf (2011) Flow-induced reconfiguration of buoyant and flexible aquatic vegetation, Limnology and Oceanography, 56(6): 2003-2017

- Lundh, H. (2000) Grundläggande hållfasthetslära, Instant Book AB
- Sundström, B. (1998) Handbook och formelsamling i Hållfasthetslära, E-print AB
- Vogel, S. (1996) Life in Moving Fluids: The Physical Biology of Flow, Princeton University Press